CHAPTER 18

FROM THE PRIMARY RADIATION INDUCED RADICALS IN DNA CONSTITUENTS TO STRAND BREAKS: LOW TEMPERATURE EPR/ENDOR STUDIES

DAVID M. CLOSE*

Department of Physics, East Tennessee State University, Johnson City, TN 37614, USA

Abstract: This review contains the results of EPR/ENDOR experiments on DNA constituents in the solid-state. Most of the results presented involve single crystals of the DNA bases, nucleosides and nucleotides. The emphasis is on low-temperature ENDOR results. Typical experiments involve irradiations at or near helium temperatures in attempts to determine the primary radiation induced oxidation and reduction products. The use of the ENDOR technique allows one to determine the protonation state of the initial products. Subsequent warming of the sample facilitates a study of the reactions that the primary products undergo. A summary of the results is provided to show the relevance the study of model compounds has in understanding the radiation chemistry of DNA

Keywords: Radiation Damage to DNA, EPR/ENDOR Spectroscopy, Primary Radiation Induced Products, DNA Strand Breaks

18.1. INTRODUCTION

DNA plays a central role as the major cellular target for ionizing radiation. Ionizing radiation produces lesions that differ from the continuously occurring endogenous lesions both in chemical nature and spatial distribution of the damage. The study of radiation damage to nucleic acids holds a central place in radiation biology. It is from the study of the free radical chemistry of nucleic acids that one may begin to understand the lethal effects of ionizing radiation.

18.1.1. Review Articles

There are several reviews of the radiation chemistry of both pyrimidines and purines. For example the article on the radiolysis of pyrimidines by von Sonntag and

* Corresponding author, e-mail: closed@etsu.edu

M. K. Shukla, J. Leszczynski (eds.), Radiation Induced Molecular Phenomena in Nucleic Acids, 493–529.

Schuchmann [1], and the book by von Sonntag, *The Chemical Basis of Radiation Biology* both contain an enormous amount of useful information [2]. Bernhard's review article "Solid-State Radiation Chemistry of DNA: The Bases", covers the early work in the same area as presented here [3]. The review article entitled "Radical Ions and Their Reactions in DNA Constituents: EPR/ENDOR Studies of Radiation Damage in the Solid-State" was an attempt to update Bernhard's 1981 review [4].

There are two important articles by Steenken on electron-induced acidity/basicity of purines and pyrimidines bases [5, 6]. These papers discuss the changes in the oxidation state of the DNA bases induced by electron loss or electron capture, and the influence these changes may have on the base-pair via proton transfer. These results are considered here in terms of the radicals observed in the solid-state.

A new book by von Sonntag, *Free-Radical Induced DNA Damage and Its Repair* has just appeared [7]. This new book provides thorough updates on what is currently known about the free radical chemistry of nucleic acids. This book also contains a section on irradiation in the solid-state. Since there is no need to repeat what has already been so adequately covered, *the present work will focus on the experimental techniques used to obtain the detailed structure of the primary radiation induced defects in DNA model systems, and to consider the subsequent transformations these primary radical undergo.*

18.1.2. Ionizations and Excitations

Most of the energy associated with an incident x-ray or γ-ray is absorbed by ejected electrons. These secondary electrons are ejected with sufficient energy to cause further ionization or excitations. The consequences of excitations may not represent permanent change, as the molecule may just return to the ground state by emission or may dissipate the excess energy by radiationless decay. In the gas phase, excitations often lead to molecular dissociations. In condensed matter, new relaxation pathways combined with the cage effect greatly curtail permanent dissociation. Specifically in DNA, it is known that the quantum yields for fluorescence are very small and relaxation is very fast. For these reasons, the present emphasis will be on the effects of ionizations.

The initial chemical events involving the deposition of energy in DNA are conveniently divided into two parts: (1) energy deposited in water and (2) energy deposited in the DNA itself. These are often called indirect and direct effects. Since some of the water in a cell is intimately associated with the DNA, these terms must be used with caution. The presence of DNA close to an energy deposition event in the water will affect the fate of the species produced, and, likewise, water molecules closely surrounding the energy disposition event in the DNA will modify the subsequent fate of the initial species. So the presence of each component modifies the behavior of the other.

18.1.3. Indirect Effects

The initial ionization of a water molecule produces an electron and the water radical cation. The water radical cation is a strong acid and rapidly loses a proton to the

nearest available water molecule to produce an $HO^{\bullet}$ radical and the hydronium ion H_3O^+. The electron will lose energy by causing further ionizations and excitation, until it solvates (to produce the solvated electron e^-_{aq}). In addition to the two radical species $HO^{\bullet}$ and e^-_{aq} , a smaller quantity of H-atoms, H_2O_2, and H_2 are also produced.

Of the two radical species $HO^{\bullet}$ and e^-_{aq}, the hydroxyl radical is more important in the radiation chemistry of DNA. The e^-_{aq} adds selectively to the DNA bases. The radiation chemistry of the DNA base radical anions will be discussed herein.

One often sees in the literature that "one-electron reduced bases are viewed as less important in the overall scheme since they do not lead to strand breaks". It is important to note that recent studies show that low-energy electrons (<20 eV) are able to produce single strand breaks in plasmid DNA by dissociative electron attachment (DEA) [8]. DEA is a terminal reaction for primary and secondary electrons approaching thermal energy. It is a resonant process that leads to fragmentation at the attachment site.

About 20% of the $HO^{\bullet}$ radicals interact with the sugar phosphate by H-atom abstraction and about 80% react by addition to the nucleobases. In model sugar compounds the H-abstraction would occur evenly between the hydrogens on C1′, C2′, C3′, C4′, and C5′. In DNA, H-abstraction occurs mainly at C4′ since C4′ in is the minor groove and to some extent with the C5′.

The $HO^{\bullet}$ radical is electrophilic and can interact by addition with the unsaturated bonds of the nucleobases. For the pyrimidines, this would be the C5 = C6 double bond. For the purines, this would include predominately C4 and C8 addition, with a minor amount of C5 addition.

18.1.4. Direct Effects

Since there is such an imprecise division between direct and indirect effects in the literature, some experimental results are presented to clarify this situation. Basically, one cannot detect $HO^{\bullet}$ radicals at low DNA hydrations (ca. 10 waters per nucleotide). This means that in the first step of ionization, the hole produced in the DNA hydration shell transfers to the DNA. It is impossible to distinguish the products from the hole or electron initially formed in the water from the direct effect damage products. For this discussion, direct type damage will be considered to arise from direct ionization of DNA or from the transfer of electrons and holes from the DNA solvation shell to the DNA itself.

18.1.5. Focus of this Chapter is on Direct-Type Damage

Von Sonntag has estimated that the direct effects contribute about 40% to cellular DNA damage, while the effects of water radicals amount to about 60% [2]. A paper by Krisch et al. on the production of strand breaks in DNA initiated by $HO^{\bullet}$ radical attack has the direct effects contribution at 50% [9].

Indirect-type damage is much better characterized, both quantitatively and mechanistically, than its direct-type counterpart. Since indirect-type damage has been

thoroughly reviewed by von Sonntag [2] and by O'Neill [10], *the emphasis of the present chapter will be on direct-type damage, mainly in the solid-state (single crystals)*.

The results of detailed electron paramagnetic resonance/electron nuclear double resonance (EPR/ENDOR) experiments on nucleic acid constituents have played a major role in understanding the primary radiation effects (radical cations and radical anions) produced by ionizing radiation. While most of the high resolution EPR/ENDOR experiments were conducted in the 1980s, there has recently been renewed interest in this work by those doing theoretical calculations on the structures of free radicals. In many cases calculations of radical structures agree well with the experimental assignments. However a few discrepancies have been noted. Some of the discrepancies stem from not understanding how free radical assignments are actually determined by the experiments. It therefore is important to describe in detail what the experiments actually measure, and to discuss the confidence level of the experimental assignments.

The aim of the present review is: (1) to outline the experimental techniques used to explore the primary radiation induced defects in nucleic acid constituents in the solid-state, (2) to provided an updated review of what is currently known about these primary induced radiation defects in DNA, (3) to consider the transformations the primary radicals undergo in order to look at biologically relevant lesion such as strand breaks, (4) to see how theoretical calculations are currently being used to assist in making free radical assignments, and finally, (5) to look at unsolved problems and make suggestions for future work.

18.2. DISTRIBUTION OF INITIAL DIRECT-TYPE DAMAGE IN DNA AND DNA MODEL COMPOUNDS

Ionizing radiation produces nonspecific ionizations; it ionizes DNA components approximately in direct proportion to the number of valance electrons. Using thymidylic acid as an example, the percentages of the total valence electrons are T (43%), dR (30%) and PO_4 (27%). The final damage is not a random distribution among these three components. Rather one finds radical anions exclusively on the bases and radical cations mostly on the bases. In DNA the radiation damage is not randomly distributed amongst the bases. At low temperatures (4–10 K) one finds the radical anions initially trapped at cytosine and upon warming to 77 K at thymine. The radical cations are localized mostly on guanine (which has the lowest gas-phase ionization potential).

The low temperature EPR experiments used to determine the DNA ion radical distribution make it very clear that electron and hole transfer occurs after the initial random ionization. What then determines the final trapping sites of the initial ionization events? To determine the final trapping sites one must determine the protonation states of the radicals. This cannot be done in an ordinary EPR experiment since the small hyperfine couplings of the radicals only contribute to the EPR linewidth. However, detailed low temperature EPR/ENDOR experiments

can be used to determine the protonation states of the low temperature products [4]. These protonation/deprotonation reactions are easily observed in irradiated single crystals of the DNA base constituents. *As the results of these experiments discussed below will show, the positively charged radical cations tend to deprotonate and the negatively charged radical anions tend to protonate.*

To predict which of the initial ionization events will recombine, and which ones will lead to a stably trapped radical, one must consider the molecular environment. For example, after irradiation, 1-MethylCytosine (1-MeC) is known to have a very low free radical yield, so it is argued that a large percentage of the initial radicals formed by the ionizing radiation must recombine. The hydrogen bonding network of 1-MeC does not favor long range proton displacements [11]. Consequently there are no energetically favorable paths which would promote the separation of unpaired spin and charge, leaving the initial sites prone to recombination. On the other hand, in many of the systems considered here, there are efficient pathways for returning ionization sites to their original charge states, thereby effectively inhibiting recombination. As a consequence, *many of the radiation induced defects reported are not the primary radiation induced events, i.e. native cations or anions, but rather neutral products, (deprotonated cations or protonated anions) which are less susceptible to recombination.*

18.3. LOW TEMPERATURE EPR/ENDOR EXPERIMENTS

If one is interested in the primary radiation events, such as electron removal or electron capture, the samples must be cooled to liquid helium temperatures. Most of the experiments described here therefore involved irradiations of samples at low temperatures, followed by subsequent warming under controlled conditions, to study the transformations these primary radicals undergo.

18.3.1. Experimental Considerations

The EPR/ENDOR measurements described here have been performed on single crystals which are accurately oriented with an x-ray precession camera, x-ray irradiated, and observed at ca. 10 K. The schematic diagram of the X-band EPR apparatus is shown in Figure 18-1 [12]. This cavity is a modification of one previously described by Weil et al. [13]. The EPR cavity is essentially a cast epoxy, wire wound TE011 cylindrical cavity with external 100 kHz modulation coils. The Cryo-Tip portion of the cavity can be raised 6 cm for x-irradiation and subsequently lowered into the microwave cavity for EPR measurements [14]. In the microwave cavity the lowest temperature of the sample is approximately 6 K. However in the irradiation position the lowest temperature is about 10 K because the sample is not as effectively heat-shielded from the room temperature vacuum shroud.

There is of course commercial EPR/ENDOR apparatus that allows for low temperature studies. However for the work described here, it is necessary to irradiate and observe the sample at helium temperatures. There is no commercial

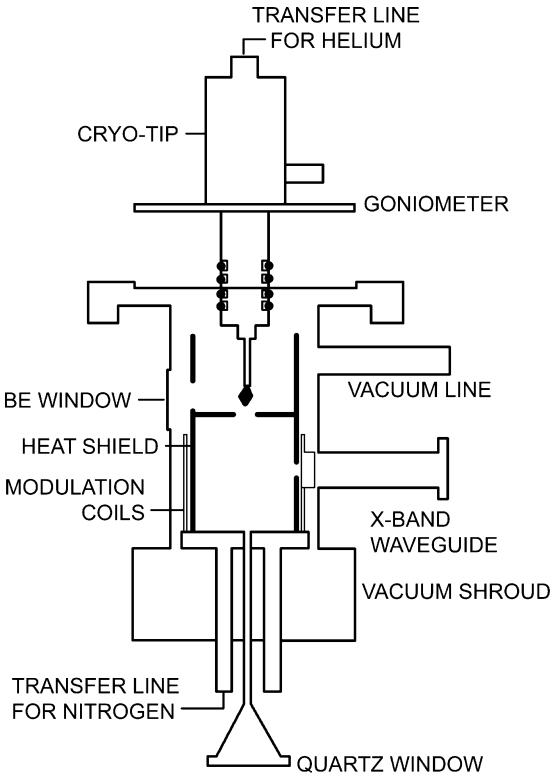

Figure 18-1. Schematic diagram of the X-band EPR apparatus for the 6 K X-irradiation and EPR measurements. The crystal is cemented to an OFHC copper pedestal that is part of an Air Products Heli-Tran system. The diagram shows the crystal in the irradiation position. After irradiation the crystal is lowered in a cylindrical EPR cavity. The cavity is cooled to 77 K to serve as a heat shield. (Reprinted with permission from ref. [12], J. Chem. Phys. © (1981) American Physical Society)

EPR/ENDOR spectrometer apparatus that allows for irradiation of samples at helium temperatures. Therefore one has to use apparatus similar to the home-made Cryo-Tip arrangement as described above, or a Janis Dewar (which has irradiation ports) with a homemade EPR cavity as described by Bernhard and co-workers [15].

18.3.2. EPR Data Analysis

The theory for analyzing anisotropic hyperfine couplings can be found in standard EPR books by Atherton [16], by Wertz and Bolton [17], or from the original papers by McConnell et al. [18, 19] or by Miyagawa and Gordy [20]. What follows here is the treatment specifically for the analysis of single crystal data with the goal of identifying free radical products.

Anisotropic proton hyperfine couplings are measured by rotating the crystals in the external magnetic field. From hundreds of angular measurements various proton hyperfine couplings are obtained as follows. EPR data are analyzed using the spin Hamiltonian (**A** in MHz)

$$H_{\mathrm{EPR}} = \beta \mathbf{H}_o \cdot \mathbf{g} \cdot \mathbf{S} + \Sigma_i \mathbf{S} \cdot \mathbf{A}^i \cdot \mathbf{I}^i + \Sigma_i g_n \beta_n \mathbf{H}_o \cdot \mathbf{I}^i \tag{18-1}$$

Where β is the Bohr magneton, $\mathbf{H}_o$ is the applied magnetic field**, g** is the g-tensor**, S** is the electron spin**, I** is the nuclear spin, g_n and β_n.are the nuclear splitting factor and the nuclear magneton. The hyperfine coupling tensor **A** consists of an isotropic contact interaction

$$(8\pi/3) g_e \beta_e g_n \beta_n \rho(0) \tag{18-2}$$

where $\rho(0)$ is the spin density at the nucleus of interest, and an anisotropic dipolar interaction between the unpaired electron and neighboring nuclear spins

$$-g_e \beta_e g_n \beta_n \int \rho(\mathbf{r}_j)(\mathbf{r}_j^2 - \mathbf{r}_j \mathbf{r}_j)/\mathbf{r}_j^5 \tag{18-3}$$

At microwave frequencies the first term in Eq. (18-1) predominates allowing the approximation **S** is quantized along the unit vector **k**, where $\mathbf{k} = \mathrm{H} \cdot \mathbf{g}/|\mathrm{H} \cdot \mathbf{g}|$. With this approximation off-diagonal elements resulting from components of **S** perpendicular to $\mathbf{H_o}$ can be neglected. Since there are no terms in Eq. (18-1) connecting different nuclear spins, it follows that the spectrum and intensity pattern for each nucleus can be analyzed independently of the other nuclei. Equation (18-1) may then be written as

$$H_{\mathrm{EPR}} = \beta \mathbf{H_o} \cdot \mathbf{g} \cdot \mathbf{k} \mathbf{S_z} + \Sigma_i \mathbf{S_z} \cdot \mathbf{A}^i \cdot \mathbf{I}^i + \Sigma_i g_n \beta_n \mathbf{H_o} \cdot \mathbf{I}^i \tag{18-4}$$

For the case $S = 1/2$, $I = 1/2$, Eq. (18-2) gives rise to an EPR spectrum consisting of two doublets (d^+ and d^-) centered at $\beta \mathbf{H_o} \cdot \mathbf{g} \cdot \mathbf{k}$. Their splittings and intensities are given as

$$\begin{aligned} d^+ &= (A_+ + A_-)/2,\ d^- = (A_+ - A_-)/2,\ I^+ = \cos^2 \xi/2,\ I^- = \sin^2 \xi/2, \text{ where} \\ \cos \xi &= (A_+ + A_-)/A_+ A_- \text{ and } A_\pm = |\pm 1/2 \mathbf{k} \cdot \mathbf{A} - \boldsymbol{\gamma} \mathrm{H}|. \end{aligned} \tag{18-5}$$

When EPR data are taken at X-band (9,500 MHz) the intensities of the so-called forbidden transitions, d^- here, are small and often neglected. This amounts to using only the first two terms in Eq. (18-1). However for small samples it is often necessary to use higher microwave frequencies (K-band, 24,000 MHz, Q-band, 35,000 MHz, or V-band, 75,000 MHz). In these experiments it is important to include the third term in Eq. (18-1), the nuclear Zeeman term.

Figure 18-2 shows an energy level diagram of the d^+ and d^- transitions. As shown, d^+ involves an electronic transition from $M_s = -1/2$ to $M_s = +1/2$, while

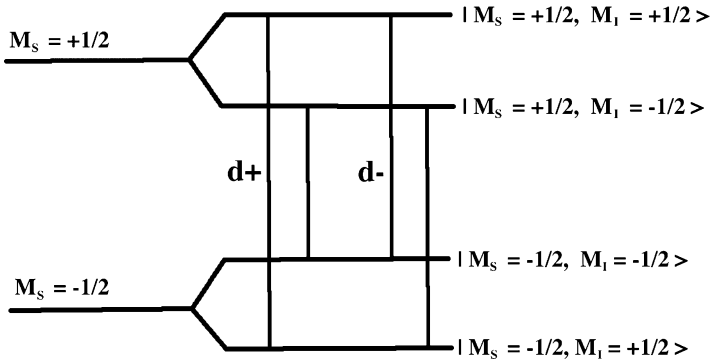

Figure 18-2. EPR energy level diagram for an electron $M_s = \pm$ 1/2 in the local magnetic field of a proton $M_I = 1/2$. The first set of transitions, d^+, involve an electronic transition from $M_s = -1/2$ to $M_s = +1/2$. The so-call "forbidden transitions", d^-, involve the simultaneous absorption of two photons as in the transition from $| M_s = -1/2, M_I = +1/2 >$ to $| M_s = +1/2$ to $M_I = -1/2 >$

d^- involves the simultaneous absorption of two photons as in the transition from $| M_s = -1/2, M_I = +1/2 >$ to $| M_s = +1/2, M_I = -1/2 >$

Equation (18-2) is nonlinear in the A_{ij}, requiring that a nonlinear optimization routine be employed to determine the best estimate of **A.** It is usually assumed that in each crystallographic plane in which data are collected the axes are exactly localized. This is seldom true for the raw data set; but in practice the inclusion of a set of adjustment angles of rotation as additional variational parameters, each an angle of rotation about the normal to an experimental plane, yields rather accurate axes orientations. One must compute a set of A_{ij} such that the function $\phi = (a_i - \hat{a}_i)^2 W_i$ is minimized. The a_i's are the data, $\hat{a}_i$'s are the calculated values, and the W_i's are the weight of the data points. Initial estimates of A_{ij} can be chosen by inspection or by use of the procedure used by Lund and Vänngård [21]. In the nonlinear least-squares procedure, the six independent elements of the **A** and **g** tensors, and three independent angles, were simultaneously varied to derive tensors which best fit the EPR data. In addition one obtains a variance-covariance matrix which may be used to calculate confidence levels in correlating the directions of eigenvectors with the direction of molecular reference vectors. Calculations of directions in the undamaged molecule were performed with a modified version of the x-ray crystallographic program ORFFE [22].

From the direction cosines associated with each coupling, comparisons can be made with specific molecular directions known from the x-ray crystal structure, in particular enabling the identification of the major sites of unpaired spin density. Examples of studies to obtain free radical assignments are included.

Figure 18-3a shows a typical EPR spectrum of a single crystal of adenosine, x-irradiated and observed at 10 K. This spectrum is obviously complex and not easy to resolve. The problem being that there are overlapping spectra from several radicals. It was therefore necessary to use several techniques to improve the spectral resolution.

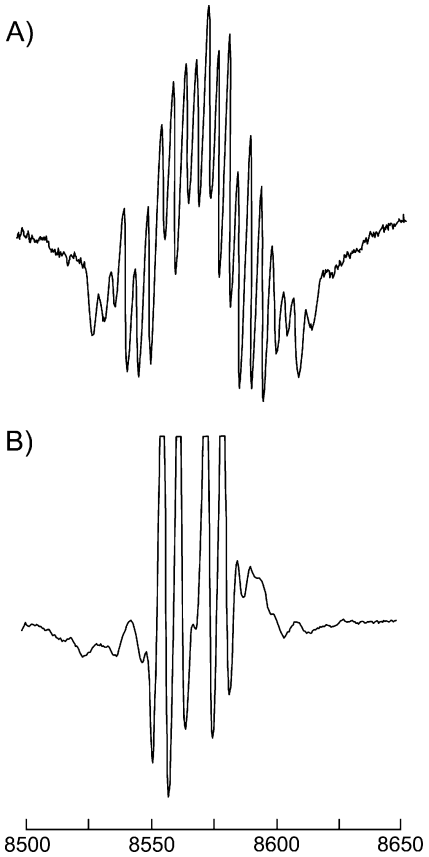

Figure 18-3. (A) K-band EPR spectrum of a single crystal of adenosine, x-irradiated and observed at 10 K. The external magnetic field H_o is 20° from the crystallographic a-axis in the ac* plane. Field units are in Gauss. (B) EPR spectrum of a single crystal of adenosine x-irradiated at 10 K, warmed to 40 K, and observed at 10 K. H_o is 35° from the crystallographic c*-axis in the ac* plane. (Reprinted with permission from ref. [30], Radiation Research © (1981) Radiation Research Society.)

18.3.3. Spectral Resolution

If two radicals exist with different g-tensors, the spectrum may be partially resolved by going to higher magnetic fields. Dramatic separations have been shown in a paper by Hüttermann et al. [23] comparing spectra at X-band (9.5 GHz) and at 245 GHz using the high field EPR spectrometer at Grenoble.

A second technique to resolve complicated spectra involves heating or aging an irradiated sample with the hope of removing one paramagnetic center. Figure 18-3b shows the effect of heating the crystal to 40 K. One sees now that one radical has disappeared, leaving a much simpler four line EPR spectrum. Often times the microwave power saturation of two overlapping EPR signals differ. Then one

can merely increase the microwave power level to selectively power saturate one of the signals.

Isotopic substitution (^{13}C,^{2}D,^{15}N) can often be used to resolve complicated spectra. For example, if a labile proton is replaced with a deuterium, the proton isotropic hyperfine coupling is reduced by a factor 6.51. This technique was used in the adenosine study discussed in Section 18.3.5.1, and in the study of the guanine cation (Section 18.3.5.3). EPR spectra of a normal crystal of guanine:HCl:H_2O, and of the same crystal grown from DCl:D_2O are shown in Figure 18-11. Most of these techniques are easy to try. If they don't succeed however, or if one is interested in measuring small hyperfine couplings, then one needs to consider the ENDOR technique.

18.3.4. ENDOR

ENDOR (Electron Nuclear Double Resonance) involves the simultaneous application of a microwave and a radio frequency signal to the sample. This is a technique invented by Feher in 1956. The original studies were on phosphorous-doped silicon. A description of the experimental results and apparatus used is presented in two Physical Review articles [24, 25]. An excellent treatment of EPR double resonance techniques and theory is given in the book by Kevan and Kispert [26]. What follows here is the theory and application of ENDOR used the in analysis of single crystal data with the goal of identifying free radical products in DNA constituents.

An EPR/ENDOR energy level diagram is shown in Figure 18-4. In these experiments an EPR line is selected (locking the magnetic field on a particular EPR line) and saturated the line by increasing the microwave power. Then radio frequency power is applied to the sample and swept over the range of the various hyperfine couplings (typically 10–100 MHz). Since the microwave power to the original EPR line has been increased, the peak-to-peak signal height has been decreased. An ENDOR transition is observed when the peak-to-peak signal height of the EPR line increases.

Figure 18-5 shows a block diagram of the ENDOR apparatus. This equipment was first used in conjunction with a Varian E-12 EPR spectrometer, but is meant to show the general features of apparatus that could be used with any EPR spectrometer. The EPR cavity (Figure 18-1) was modified for the ENDOR experiment with the inclusion of a hair-pin loop around the Cryo-Tip. The loop is fed with a 50 Ω transmission line from a 50–100 Watt broadband radio-frequency (rf) amplifier and is terminated with a non-inductive, water cooled 50 Ω resistance.

In the examples presented below there are figures of strong ENDOR signals obtained from single crystals irradiated and examined at helium temperatures. One must not get the idea that it is easy to obtain ENDOR signals from every sampled examined. Often there are conditions present involving the electronic and nuclear relaxation terms that preclude ENDOR detection even with 100's of watts of rf power. The conditions that must be met to obtain ENDOR signals are covered in the standard textbooks [26].

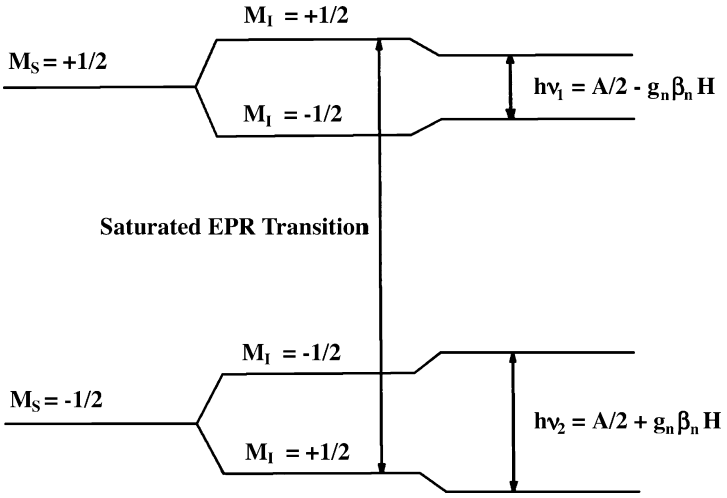

Figure 18-4. ENDOR energy level diagram for an electron $M_s = \pm 1/2$ in the local magnetic field of a proton $M_I = 1/2$. To observe an ENDOR transition, the external magnetic field H_o is positioned on an EPR line, in this case the transition from $| M_s = -1/2, M_I = +1/2 >$ to $| M_s = +1/2, M_I = +1/2 >$. Then a radio-frequency transmitter is scanned through the various "NMR" frequencies (typically 10–100 MHz). This diagram shows two ENDOR transitions of energy $h\upsilon_1$ and $h\upsilon_2$ that correspond to the hyperfine couplings of a nuclear spin with $M_I = \pm 1/2$

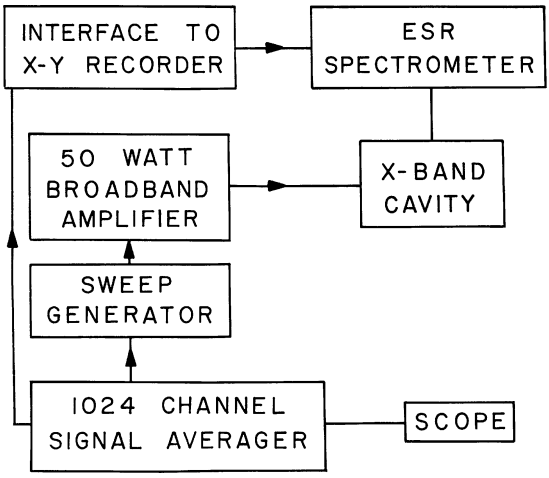

Figure 18-5. Block diagram of the ENDOR apparatus

18.3.4.1. ENDOR data analysis

ENDOR data are analyzed by a two step procedure. Input data obtained from the equation

$$A(\theta, \phi) = 2.0(\boldsymbol{\nu}_{\mathrm{ENDOR}} - (1/h)g_n\beta_n|\mathbf{H_o}| \tag{18-6}$$

were used to generate a trial A tensor using Schonland's method [27]. A non-linear least squares procedure was then used to generate a refined A tensor which best fit the actual ENDOR data from each crystallographic plane to the ENDOR Hamiltonian

$$H_{\mathrm{ENDOR}} = |((\mathbf{l}\cdot\mathbf{A})/2 \pm (1/h)g_n\beta_n\mathbf{H_o})|. \tag{18-7}$$

18.3.4.2. Field-swept ENDOR

As discussed above, in the EPR experiments with overlapping spectra one is often faced with resolution problems. A similar situation occurs in the ENDOR experiments when there are too many ENDOR lines. The obvious problem becomes how to assign ENDOR lines to the various free radicals present. In some cases it is possible to modify the EPR/ENDOR experiment to solve this problem. The technique involves sitting on an ENDOR line and sweeping the magnetic field while recording the EPR signal. While the EPR signal may be broad, its overall pattern and spectral extent will be different for each individual radical present. Wonderful examples of the field-swept ENDOR technique can be seen in an ENDOR study of a steroid [28]. A figure in this article shows an X-band ENDOR spectrum with 15 lines. Field-swept ENDOR spectra from three sets of distinct EPR spectra were obtained. In some cases the FSE spectra are not as distinct. For example, one of the FSE spectra observed recently in a co-crystal of N-Formylglycine:Cytosine is not very sharp, but was still helpful in assigning the ENDOR lines to different radicals [29].

18.3.4.3. Combined EPR and ENDOR results

In the actual experiments, EPR spectra are also recorded at every orientation, from which one can make good estimates of anisotropic nitrogen hyperfine couplings which are not normally detected in the ENDOR experiments. In most cases complicated single crystal (and even powder) EPR spectra can be faithfully reproduced with the accurate proton couplings obtained from the ENDOR experiments and the nitrogen hyperfine couplings obtained from the EPR spectra. Examples of these combined results will be presented.

The purpose of obtaining all this information is to present reasonable free radical models for the primary oxidation and reduction products observed in the irradiated crystals. This begins with, and is usually based on, the precise information about major sites of spin density. There are however, some problems in dealing with all of the small hyperfine couplings obtained from the ENDOR data. This could mean, for example, that one may have problems with establishing precisely what

the protonation state of a given model is. One procedure used to solve this problem is to repeat the entire experiment with partially deuterated single crystals to learn which of the many small hyperfine couplings are at exchangeable bonding sites. As shown here, one may also use theoretical calculations to aid in making suitable radical assignments.

18.3.5. Examples of Detailed Data Analysis

18.3.5.1. Analysis of an irradiated single crystal of adenosine

The first example considered involves a low temperature study on a single crystal of the nucleoside adenosine [30]. A typical K-band (24 GHz) EPR spectrum of a single crystal of adenosine, x-irradiated and observed at 10 K was shown in Figure 18-3a. This spectrum consists of numerous hyperfine lines with spectral extent of >80G. Very little information could be obtained from such spectra since it proved impossible to follow the angular variations of the individual hyperfine lines as the crystal was rotated in the external magnetic field. A typical ENDOR spectrum (Figure 18-6) showed five sets of hyperfine couplings from 35–70 MHz (the proton NMR frequency being 35.6 MHz at the K-band microwave frequency used). The angular variations of these five couplings in three orthogonal crystallographic planes are shown in Figure 18-7. These hyperfine couplings can be associated with two distinct free radicals by the following procedure.

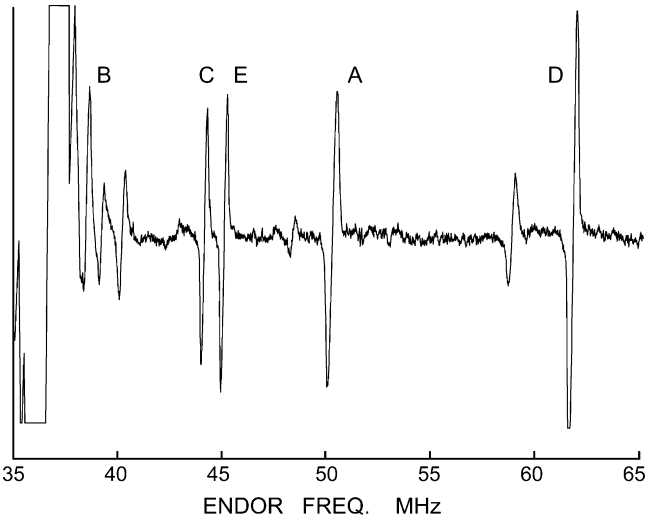

Figure 18-6. K-band ENDOR spectrum of a single crystal of adenosine x-irradiated and observed at 10 K. The spectrum was observed for H_o parallel to the crystallographic c*-axis. The "distant" ENDOR signal is at 36.5 MHz. (Reprinted with permission from ref. [30], Radiation Research © (1981) Radiation Research Society.)

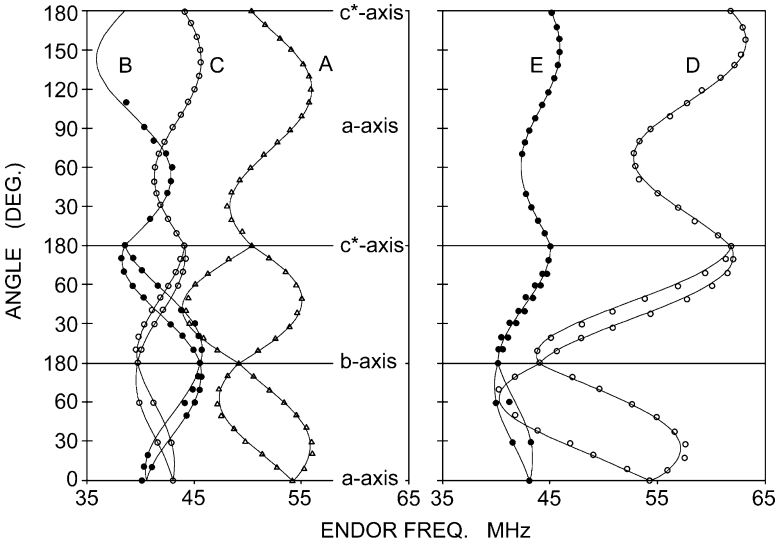

Figure 18-7. Angular variations of the ENDOR spectra in three orthogonal crystallographic planes. Points marked are actual data, while the curves connecting these points were drawn from the tensors listed in Table 18-1. (Reprinted with permission from ref. [30], Radiation Research © (1981) Radiation Research Society.)

If the crystal is warmed to ca. 40 K, ENDOR lines A, B and C (Figure 18-6) abruptly disappears. On cooling back to 10 K, the EPR spectrum is dominated by two distinct intense doublets at the orientation shown in Figure 18-3b. The small splitting of 7.25 G here corresponds to an ENDOR line at 46.6 MHz (ENDOR line E in Figure 18-6) and the 18.35 G splitting corresponds to a 62.2 MHz ENDOR line (line D in Figure 18-6). These two ENDOR lines then are to be associated with a radical designated Radical II below. Likewise, ENDOR lines A, B, and C are associated with Radical I. Field–swept ENDOR experiments were used to confirm each of these line assignments.

18.3.5.1.1. Radical I The first three hyperfine coupling tensors in Table 18-1 were derived by following the angular variations of ENDOR lines A, B and C (Figure 18-6). It can be seen that for each hyperfine coupling tensor the intermediate principal axes is normal to the adenine base-plane suggesting a π-radical. Figure 18-8 shows the structure of an sp^2 >C-H π-radical with the principal direction values of the anisotropic hyperfine coupling superimposed. One sees that the direction of A_{min} is along the C-H bond, the direction of A_{mid} is the direction of the unpaired π-orbital, and A_{max} is in a direction perpendicular to the first two directions.

The hyperfine coupling associated with Line A is characteristic of an α-proton bonded to C2 with π-spin density at the carbon. The fit between the direct cosine associated with A_{min} and the computed direction of C2-H is excellent, they differ

Table 18-1. Hyperfine Coupling Tensors for Radicals I and II Observed in Adenosine

	Principal value (MHz)	Direction cosines			$\Delta\psi$[a]
Radical I					
	46.00 ±0.16	−0.6720	−0.5050	0.5416	
C2-H	27.77 ±0.14	0.7394	−0.4170	0.5287	
	15.71 ±0.16	−0.0412	0.7557	0.6536	
		(−0.0066)	(0.7424)	(0.6699)[b]	2.3 ±0.5°
	$A_{iso} = 29.83$				
		0.2661	0.9260	−0.2677	
	19.20 ±0.26	0.7679	0.3715	0.5218	
N3-H	11.61 ±0.20	−0.5827	0.0667	0.8100	
	−1.37 ±0.22	(−0.5755)	(0.0741)	(0.8145)[c]	0.6 ±0.6°
	$A_{iso} = 9.81$				
	18.40 ±0.06	−0.6116	0.0122	0.7911	
C8-H	10.40 ±0.08	0.7147	−0.4205	0.5590	
	5.46 ±0.08	0.3395	0.9072	0.2484	
		(0.3550)	(0.8845)	(0.3026)[d]	3.5 ±0.6°
	$A_{iso} = 11.42$				
Radical II					
	55.91 ±0.22	−0.4459	−0.2244	0.8665	
N6-H	37.38 ±0.20	0.7807	0.3759	0.4992	
	8.44 ±0.27	−0.4378	0.8991	0.0076	
		(−0.4547)	(0.8822)	(0.1227)[e]	6.7 ±0.3°
	$A_{iso} = 33.91$				
	18.76 ±0.08	−0.5004	0.0870	0.8014	
C8-H	12.07 ±0.09	0.7987	−0.3376	0.4980	
	6.50 ±0.11	0.3341	0.9373	0.0995	
		(0.3550	(0.8845)	(0.3026)[d]	12.1 ±0.6°
	$A_{iso} = 12.44$				

[a] $\Delta\psi$ is the angle between the direction given for a special principal value and the expected direction cosine computed from the coordinates of the native molecule. The error listed for these angles are at the 95% confidence level; [b] The expected direction of the C2-H bond (inplane bisector of the N1-C2-N3 angle); [c] The expected direction of the N3-H bond (inplane bisector of the C2-N3-C4 angle); [d] The expected direction of the C8-H bond (inplane bisector of the N7-C8-N9 angle); [e] The expected direction of the N6-H1 bond.

by only 2°. In the same manner it can be seen that coupling B is characteristic of an α-proton bonded to nitrogen N3 with a π-spin density at the nitrogen.

The third line seen in some of the ENDOR spectra was not as easy to analyze. It can be seen in Figure 18-7 that this line closely follows another stronger ENDOR line associated with Radical II. However enough data were available to determine that line C is to be associated with a small C8-H coupling. Again the fit between the expected direction and the computed direction of A_{min} is excellent (Table 18-1).

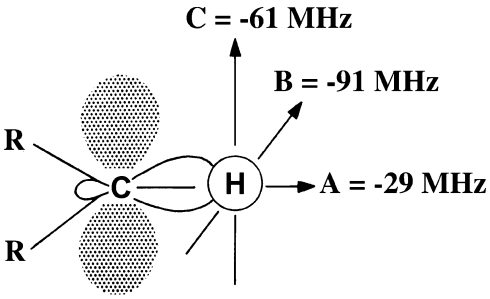

Figure 18-8. Proton hyperfine couplings for a planar $>C-H_{\alpha}$ fragment showing the principal values and directions of the proton anisotropic hyperfine coupling

From the results presented in Table 18-1, the C2, N3 and C8 spin densities may be estimated from the formula

$$A_{iso} = \rho(C2)Q_{CH} \tag{18-8}$$

Q-values of -80 MHz for both the imidazole carbon [31] and the nitrogen [32] were used. A Q-value of -72 MHz has been suggested for the pyrimidine carbon [33]. The results are $\rho(C2) = 0.41$, $\rho(C8) = 0.14$ and $\rho(N3) = 0.12$. The model proposed for Radical I is the N3 protonated adenine anion $A(N3+H)^{\bullet}$, is shown in Figure 18-9.

18.3.5.1.2. Radical II The last two hyperfine coupling tensors in Table 18-1 are associated with Radical II. This radical remains after Radical I decays at ca. 40 K. Radical II is present in crystals warmed to 100 K. It can be seen that for each hyperfine coupling tensor that the intermediate principal value is normal to the adenine ring plane, again suggesting a π-radical. The hyperfine coupling associated with ENDOR line D is characteristic on an α-proton coupling resulting from π-spin density on a nitrogen. This hyperfine line is clearly missing in experiments conducted on deuterated crystals. The best correlation between the direction of A_{min} and computed >X-H directions was found for the N6-H direction (they differ by 7°).

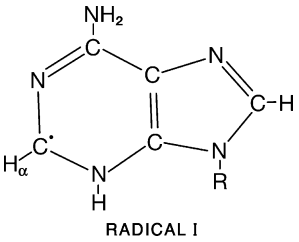

Figure 18-9. Radical I, the N3 protonated adenine anion $A(N3+H)^{\bullet}$. (Reprinted with permission from ref. [30], Radiation Research © (1981) Radiation Research Society.)

The angular variation of ENDOR line E in Figure 18-6 closely parallels Line C (assigned above to a small C8-H hyperfine coupling). From the results one can see that for line E the diagonal elements of the hyperfine coupling tensor are typical of an α-proton coupling resulting from a small π-spin density on a carbon. The direction of A_{min} however is not as close to the computed direction of C8-H as one would expect. It seems safe to conclude however that line E is associated with a small C8-H coupling. From the results present in Table 18-1, the C8 and N6 spin densities may be estimated to be ρ(C8) = 0.162 and ρ(N6) = 0.424. The model proposed for Radical II is the N6 deprotonated adenine cation A(N6-H)• shown in Figure 18-10.

In the analysis of the ENDOR data for Radical I all three hyperfine coupling tensors fit the expected directions of the crystal structure very closely. These tensors were produced by fitting >90 accurately measured data points to theoretical equations with a total rms error of ca. 0.25 MHz. For Radical II the tensors are just as accurate, but the expected directions are off by ca. 10°. It can be seen that the A_{mid} direction for both the >N6-H and C8-H couplings are both 8.3° from the computed ring perpendicular. This suggests that there is some slight deviation from planarity for this radical.

From these results one can see the incredible power of the combined EPR/ENDOR experiment. While the EPR spectrum of irradiate adenosine had rather narrow lines, the spectrum was unresolved due to the overlap of several radicals. The ENDOR spectra were easy to follow for complete rotations about all three crystallographic axes. Analysis of the ENDOR data yielded accurate anisotropic hyperfine tensors that could be related to two different free radicals. From these results one can confidently say that Radical I is the N3 protonated adenine anion A(N3+H)•, and Radical II is the N6 deprotonated adenine cation A(N6-H)•. With ENDOR data one is able to determine the protonation state of a radical, and if care is taken in the analysis, to even discern slight deviations from planarity of radicals.

18.3.5.2. Detailed analysis of a cytosine reduction product (1MeC)

Here it is interesting to continue with the discussion of using the ENDOR data to discern radical geometry. Results for the cytosine reduction product observed in irradiated single crystals of 1-MethylCytosine:5-FluoroUracil are shown in Table 18-2 [34]. First one notes the three principal values of the hyperfine coupling tensor. For an ordinary π-electron radical with unit spin density on the central

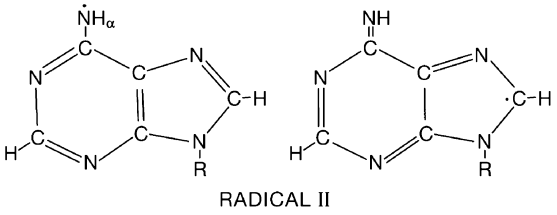

RADICAL II

Figure 18-10. Radical II, N6 deprotonated adenine cation A(N6-H)•. (Reprinted with permission from ref. [30], Radiation Research © (1981) Radiation Research Society.)

Table 18-2. Hyperfine Coupling Tensors for the 1-MeC Reduction Product

	Principal value (MHz)	Direction cosines			$\Delta\psi^a$
Radical I					
	-62.47 ± 0.17	0.5140	-0.4883	-0.7052	
C6-Hα	-34.58 ± 0.15	0.7847	-0.0643	0.6165	
	-18.74 ± 0.12	(0.7943)	(-0.0315)	$(0.6068)^b$	$2.05 \pm 0.5°$
		0.3464	0.8703	-0.3502	
		(0.3003)	(0.8885)	$(-0.3470)^c$	$2.80 \pm 0.3°$
	$A_{iso} = -38.60$				

[a] $\Delta\psi$ is the angle between a specific principal value and the expected direction computed from the coordinates of the native molecule; [b] The expected direction of the C6 2pπ orbital (the perpendicular to the C5-C6-N1 plane); [c] The expected direction of the C6-H_α bond (the in-plane bisector of the C5-C6-N1 angle).

carbon, the principal values are known to be ca. 91, 61, and 29 MHz as shown in Figure 18-8. One sees that the principal values of the >C6-H_α hyperfine coupling tensor listed in Table 18-2 are approximately 50% of these numbers, reflecting the fact that the unpaired spin density at C6 is approximately 50%. The actual spin density ρ(C6) was determined to be 0.53, in close agreement with that observed in other cytosine derivatives [4].

It is important to note that the proportional relationship between A_{max}, A_{mid}, and A_{min} for these couplings is the same for 100% spin density, and for the present case with approximately 50% spin density. When this is so it indicates that there is no rocking motion at the radical site. This is good evidence therefore that the radical site is essentially planar. The best evidence for radical planarity comes from the analysis of the direction cosines associated with each principal values of the hyperfine coupling tensor. The direction of A_{min} (Table 18-2) is known to be associated with the direction of the >C-H bond, while the direction associated with the A_{mid} indicates the direction of the π-electron orbital. These directions are easily calculated from the crystal structure, and are included in Table 18-2. One sees that the direction associated with A_{mid} deviates only 2.0° from the computed perpendicular to the ring plane, while the direction of A_{min}, deviates only 2.8° from the computed direction of the C6-H bond. The errors listed on these values are at the 95% confidence level. This is very clear evidence that the radical shown here is planar in the solid-state. Any torsional motion of the C6-H would lead to asymmetries of the hyperfine coupling tensor, and would not produce the observed agreement between the direction cosines and the known directions obtained from the crystal structure.

18.3.5.3. Search for the guanine cation

Guanine is the most easily oxidize DNA base. This means that holes, created at random sites, will move around until encountering a guanine. In order to be stably trapped on guanine, the cation will have to deprotonate. The site of deprotonation has only recently been determined. EPR/ENDOR results predicted a cation deprotonated at the exocyclic amine G(N2-H)•, while model calculations predicted a cation deprotonated at N1 G(N1-H)•.

Characterizing the guanine oxidation product has been a very difficult task. To use the power of the EPR/ENDOR techniques described herein, one needs suitable single crystals. Of course one can find hundreds of single crystals papers on guanine derivatives in the literature. However this is misleading because crystallographers prefer very small crystals. If a crystal is too big, the diffraction intensities vary artificially as the x-ray beam passes through thicker portions of the crystal. For an X-band or K-band EPR experiment one would like a crystal 3–4 mm long. It is difficult to grow crystals of guanine derivatives this size because of solubility problems.

The first crystals large enough for K-band EPR studies were grown from dilute HCl. The best crystals obtained were guanine hydrochloride monohydrate. The crystal structure of G:HCl and A:HCl were published by Broomhead in 1950 [35]. The guanine:HCl:H_2O crystals are protonated at N7. The first reports on the crystals showed the EPR spectra in Figure 18-11 [36]. There one sees a central doublet flanked by a weak anisotropic spectrum that reaches a peak spectral extent of ca. 60 G when the external magnetic field is parallel to the <c> crystallographic axes. At this orientation the EPR spectrum is dominated by two nitrogen hyperfine couplings of ca. 15 and 9 Gauss. The nitrogen spin densities were determined to be $\rho(N3) = 0.283$ and $\rho(N2) = 0.168$. Such nitrogen spin densities are common for oxidation products. It is believed that this radical is best represented as the N7 deprotonated guanine cation as shown in Figure 18-12.

Of course guanine in not normally protonated at N7. The work described on the guanine:HCl:H_2O single crystals would be equivalent to the native guanine cation (Figure 18-12). It would be very unusual for an actual cation to be stably trapped. If native guanine were one-electron oxidized, it would most likely deprotonate. So when one talks about oxidation of guanine, this normally means a neutral radical species (the deprotonated guanine cation). So then the question remains, what is the structure of this species?

Crystals of 2′-Deoxyguanosine 5′-Monophosphate Tetrahydrate Disodium Salt (5′-dGMP) have a neutral guanine base. In the solid-state, oxidation of 5′-dGMP at 10 K leads to deprotonation at the exocyclic nitrogen which is characterized by $\rho(C8) = 0.175$ and $\rho(N2) = 0.33$ [37]. The same radical was detected in crystals of 3′,5′-cyclic guanosine 5′-monohydrate. In this second study, the N3 spin density was determined to be 0.31 [38]. These two studies then provide a detailed description of the amino deprotonated guanine cation G(N2-H)$^{\bullet}$.

18.3.6. Simulation of EPR Spectra from ENDOR Data

One can gain even more confidence in the experimental results by attempting to simulate the EPR spectra from the hyperfine coupling tensors. These simulations are carried out with programs outlined in two papers by Lefebvre and Maruani [39, 40]. The original code in these programs has recently been updated and expanded in collaborations with Lund and Sagstuen to include ^{14}N quadrupole couplings and the effects of microwave power saturation on forbidden transitions [41, 42]. Examples of successful simulations are presented in a recent paper on the primary radicals observed in 5′-dCMP [43].

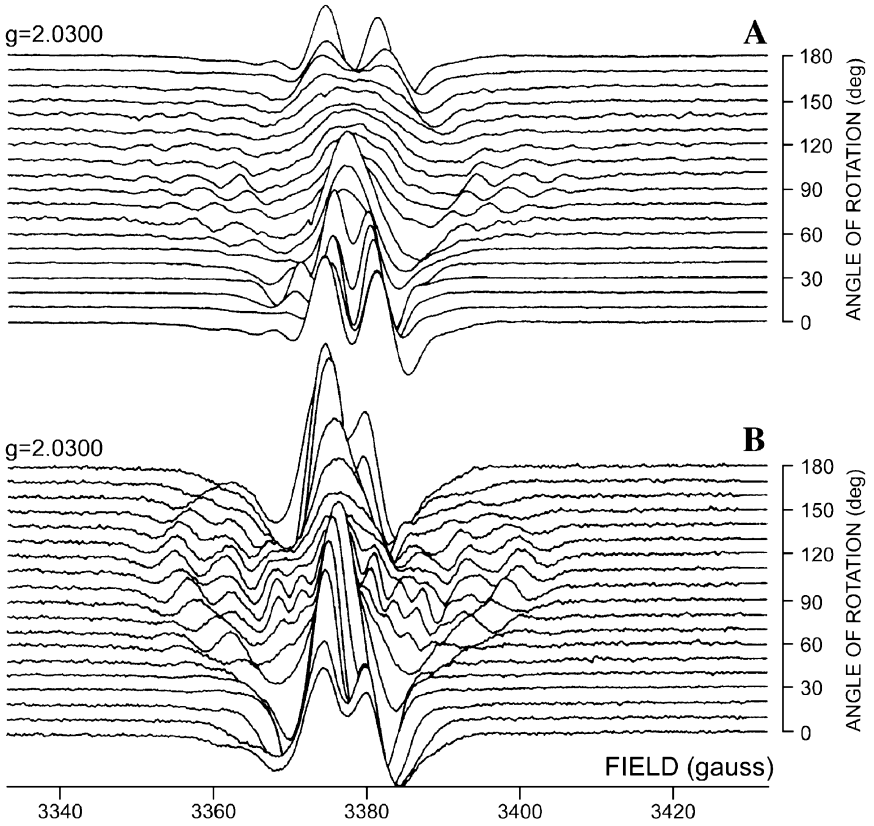

Figure 18-11. (A) EPR spectrum of a single crystal of guanine:HCl:H_2O x-irradiated and observed at 15 K for rotation about the crystallographic b-axis. The central portion of the spectrum is dominated by a broad doublet for H_o parallel to the a* crystallographic axis (0° here). The outer lines, with spectral extent reaching 57 G (best seen for H_o parallel to the c crystallographic axis) are from the guanine cation. (B) Same conditions for the guanine DCl:D_2O crystal. The spectral extent of the guanine cation EPR signal is approximately 46 Gauss for H_o 120° from the a* crystallographic axis. (Reprinted with permission from ref. [36], J. Chem. Phys. © (1985) American Physical Society.)

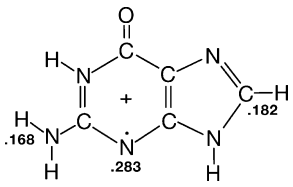

Figure 18-12. Structure of the guanine cation with spin densities ρ(N2) = 0.168 and ρ(C8) = 0.182. (Reprinted with permission from ref. [36], J. Chem. Phys. © (1985) American Physical Society.)

18.3.7. Controlled Warming Experiments

With the apparatus described in Section 18.3.1, single crystals are irradiated at helium temperatures. They are maintained at low temperature while EPR/ENDOR experiments are performed by maintaining the flow of liquid helium to the Cryo-Tip. If the gas pressure between the helium supply tank and the Cryo-Tip is reduced, the temperature can be raised in a controlled fashion. The typical radiation induced radicals discussed herein often decay as the temperature is raised to 50–100 K. So one raises the temperature in small steps while looking at the EPR spectrum for changes. When changes occur, the sample is returned to 6 K, and the experiments are repeated on the decay products. These controlled warming experiments are important in mapping out the reactions that the primary products undergo. Good examples of the use of controlled warming experiments in the study of 5′-dCMP are shown with experiments conducted between 6 K and 77 K [43].

18.4. INITIAL TRAPPING SITES OF HOLES AND EXCESS ELECTRONS OBSERVED BY LOW TEMPERATURE EPR/ENDOR EXPERIMENTS

18.4.1. Model Systems

Now that the experimental details of a few model systems have been discussed it is important to summarize the work on model systems. These include studies of irradiated nucleosides and nucleotides from which one can usually determine the detailed structures of the free radical products. The emphasis here will be to summarize the results on EPR/ENDOR studies of irradiated DNA bases at low temperatures in efforts to study the primary radiation induced defects. This summary is based on a review article published some time ago [4]. Available updates have been included here.

18.4.1.1. Cytosine

Reduction of cytosine produces a radical with sites of unpaired spin density at C2, C4 and C6. The hyperfine coupling of the unpaired spin with the C6-H_α produces a ∼1.4 mT doublet which is the main feature of the "cytosine anion" EPR signal which has been observed in various cytosine derivatives [44]. Studies of cytosine monohydrate single crystals irradiated at 10 K were performed by Sagstuen et al. [45]. ENDOR experiments detected the C6-H_α hyperfine coupling, the N3-H_α hyperfine coupling and one of the small couplings to the N4-H_2 protons (see Table 18-2). With a Q value of −72.8 MHz in Eq. (18-6), the spin density at C6 was estimated to be 0.52. From EPR measurements the nitrogen spin densities were determined to be $\rho(N3) = 0.07$ and $\rho(N4) = 0.06$. Thus the reduction product in cytosine monohydrate is the N3 protonated anion $C(N3+H)^{\bullet}$.

In this analysis it is helpful to compare the solid-state results with what is known about the redox properties of the DNA bases in solution The cytosine anion is a strong base ($pK_a > 13$) [5] and is therefore expected to rapidly protonate in solution.

It is therefore interesting to note that the protonation of the cytosine anion noted above occurs even at 10 K. Oxidation of cytosine produces a radical with sites of unpaired spin density at N1, N3 and C5.

The cytosine cation has a $pK_a < 4$ and in solution deprotonates at NH_2 [5]. In the solid-state Sagstuen et al. [45] assigned the primary oxidation radical observed in cytosine $\rho(N1) = 0.30$ and $\rho(C5) = 0.57$. Furthermore there are two small exchangeable N-H couplings whose angular variations correlate well with the exocyclic N4-H's.

Since an oxidation product on cytosine in DNA could not deprotonated at N1, it may be more relevant to look at oxidation in a nucleotide. In 5′-dCMP (with N3-H in the native molecule) oxidation produces the N3 deprotonated cation with $\rho(N1) = 0.30$ and $\rho(C5) = 0.60$ [43].

Some time ago an allyl-like radical was observed in irradiated crystals of 5′-dCMP [46]. This radical was thought to be a sugar radical, though no likely scheme was proposed for its formation. It is now appears that this radical is formed on 5-methyl cytosine impurities in these crystals. This radical forms by deprotonation of the cytosine cation, and may have important consequences in the radiation chemistry of DNA since the ionization potential of 5-methyl cytosine is lower than that of either cytosine or thymine [47]. An important point here is that deprotonation of the 5-methyl cytosine cation occurs at the C5-CH_3. This is an irreversible deprotonation, so if 5-methyl cytosine captures a hole and deprotonates, the hole is stably trapped.

18.4.1.2. Thymine

The thymine anion is only a weak base ($pK_a = 6.9$) [5]. This means that protonation of the anion may depend on the specific environment. The primary reduction product observed in the solid-state in thymine derivatives is the C4-OH protonated anion T(O4+H)• [4]. This species exhibits significant spin density at C6 and O4. Here one must distinguish between two different situations. In single crystals of thymidine the C4-OH_β proton is out of the molecular plane which gives rise to an additional 33.1 MHz isotropic hyperfine coupling [48]. A similar situation is observed in single crystals of anhydrous thymine [49]. In 1-MeT however the C4-OH_β proton is in the molecular plane and consequently the OH proton coupling is very small [48].

There is not much discussion of thymine oxidation products since they are viewed as unimportant in the radiation chemistry of DNA. The feeling being that in DNA most of the oxidation will occur on the purines. However when model systems are used, there are several known pathways that involve oxidation of the thymine base. When a thymine base is ionized, the resulting thymine cation is an acid with $pK_a = 3.6$ for deprotonation in solution [5]. The thymine cation will likely deprotonate at N3 though one must look for alternative routes for the cation to eliminate excess charge if N3 is not hydrogen bonded to a good proton acceptor. One could have reversible deprotonation of the thymine cation at N3, or irreversible deprotonation at the C5-CH_3.

In all thymine derivatives studied so far in the solid-state there is always a significant concentration of a radical formed by net H abstraction from the >C5-CH_3

group [4]. This allyl-like radical is present at helium temperatures. From studies of frozen thymine solutions it can be shown that the precursor of the allyl-like radical is the thymine cation [50].

18.4.1.3. Guanine

At the time Steenken's review article was written, the radical anion of guanine had not been fully studied in aqueous solution [5]. This was considered in a later study which showed that radical anion $G^{\bullet}-$ rapidly protonates at N3 or N7 followed by tautomerization to give a radical protonated at C8 $G(C8+H)^{\bullet}$ [51]. Many of the solid-state studies of guanine derivatives report these "H-addition" radicals even at low temperatures [37, 52].

In single crystals of 5′-dGMP the native molecule is not protonated at N7. EPR/ENDOR experiments detected a narrow doublet whose hyperfine coupling correlates with a C8-H_{α} interaction. The computed spin density was $\rho(C8) = 0.11$. This radical was unstable on warming above 10 K, and therefore it was proposed that the radical responsible was the pristine radical anion [37]. However it is possible that the guanine C6-OH protonated anion could explain these data. The guanine deprotonates at 10 K, but then the protonation reverses upon warming, leaving the original anion, which is then subject to recombination.

The guanine cation is a weak acid ($pK_a = 3.9$) [5]. Therefore deprotonation will depend on the environment. Bachler and Hildenbrand have studied the guanine oxidation product in aqueous solution of 5′-dGMP [53]. The best fit to their EPR spectra seems to be from the radical cation (guanine remains protonated at N1).

In the solid-state, oxidation of 5′-dGMP at 10 K leads to deprotonation at the exocyclic nitrogen which is characterized by $\rho(C8) = 0.175$ and $\rho(N2) = 0.33$ [37]. The same radical was detected in crystals of 3′, 5′-cyclic guanosine 5′-monohydrate. In this second study, the N3 spin density was determined to be 0.3 [38].

Some experiments have been performed on guanine molecules that were originally protonated at N7. Subsequent electron loss by this molecule leads to deprotonation at N7 yielding a radical which is equivalent to the guanine cation as discussed in Section 18.3.5.3. The experimental results from this guanine cation have $\rho(C8) = 0.18$, $\rho(N2) = 0.17$ and $\rho(N3) = 0.28$ [36].

It is not clear what the structure of the DNA cation is. The amino deprotonated product observed in 5-dGMP does not seem to fit parameters of the oxidation species observed in DNA. Recently Steenken has claimed that the one-electron oxidized species found in double stranded DNA is the radical cation [54].

It seems then that one-electron oxidized guanine in the solid-state deprotonates at the amino group. There is however no good evidence that this occurs in aqueous solution. A study of guanine derivatives in aqueous solution using pulse radiolytic techniques concluded that one-electron oxidized guanine deprotonated at N1 [55]. Early ab initio calculations on guanine concluded that $G(N1\text{-}H)^{\bullet}$ is the more stable than $G(N2\text{-}H)^{\bullet}$ [56]. However more recent DFT and molecular dynamics calculations have come to the opposite conclusion [57]. Calculations have also been performed on G:C base pairs. Hutter and Clark have concluded that proton transfer

from N1 of guanine to N3 of cytosine is unfavorable by 1.6 kcal/mole [58]. More recently, Li and co-workers have found a lower value of 1.25 kcal/mole for this proton transfer, and suggest that there is an equilibrium between the two states [59]. Also, the dipole moment of G(N1-H)$^{\bullet}$ is larger than that of G(N2-H)$^{\bullet}$, which suggests that G(N1-H)$^{\bullet}$ might be favored in an aqueous environment. Therefore the situation is that there are reliable EPR/ENDOR magnetic parameters for the amino deprotonated guanine cation, but not for the N1 deptrotonated guanine cation. Using just EPR parameters, one cannot distinguish between the N1 deprotonated guanine cation and the native guanine cation. So the next step is to determine the magnetic parameters of the N1 deprotonated guanine cation.

Jayatilaka and Nelson have recently studied single crystals of Sodium Guanosine Dihydrate [60]. The crystals are grown at high pH in NaOH. The guanine base therefore exists as an anion (N1 deprotonation). From analysis of the C8-H hyperfine coupling the authors determine that $\rho(C8) = 0.22$. No hyperfine coupling was detected from the large α-proton from the remaining amino proton. Furthermore the spectral extent of the field-swept ENDOR from this species is too narrow to be from the amino deprotonated cation. Therefore the best fit to the data is the long sought N1-deprotonated guanine cation. This study also includes a discussion of a g-tensor for the N1 deprotonated radical as well as information useful in simulating the randomly oriented EPR spectrum of this radical.

A new paper by Adhikary et al. [61] has also looked at the deprotonated states of the guanine cation. This paper first revisits the calculated stabilities of G(N1-H)$^{\bullet}$ vs. G(N2-H)$^{\bullet}$. Their calculations agree with those of Mundy et al. [57] discussed above that G(N2-H)$^{\bullet}$ is more stable than G(N1-H)$^{\bullet}$ in a non-hydrated environment. However when discrete waters of hydration are added, G(N1-H)$^{\bullet}$+7H_2O is more stable than G(N2-H)$^{\bullet}$ 7H_2O. This paper is complimented with simulations of the EPR spectra that are obtained from experimentally determined hyperfine couplings.

18.4.1.4. Adenine

The adenine anion has a $pK_a = 3.5$ [5]. After electron capture the negative charge of the adenine radical anion resides mainly on N1, N3, and N7 and therefore protonation likely occurs at one of these nitrogen's. The results in Section 18.3.5.1.1 showed that in a single crystals examined at 10 K that reduction of adenine leads to the N3 protonated adenine anion with spin densities of ca. $\rho(C2) = 0.41$, $\rho(C8) = 0.14$, and $\rho(N3) = 0.12$ [30].

The adenine cation was observed in a single crystal of adenine hydrochloride hemihydrate [62]. In this crystal the adenine is protonated at N1. After electron loss the molecule deprotonates at N1. This produces a radical that is structurally equivalent to the cation of the neutral adenine molecule with spin density on C8 and N6 ($\rho(C8) = 0.17$ and $\rho(N6) = 0.25$). The adenine cation is strongly acidic ($pK_a < 1$) [5]. This strong driving force makes the reaction independent of environmental conditions. In single crystals of adenosine [30] and anhydrous deoxyadenosine [63] the N6 deprotonated cation is observed which is characterized

by $\rho(C8) = 0.16$ and $\rho(N6) = 0.42$. The experimental isotropic hyperfine couplings are N6-H_α = 33.9 MHz, and C8-H_α = 12.4 MHz.

In single crystals of deoxyadenosine [64] the site of oxidation seems to be the deoxyribose moiety. This brings up an interesting point. In studies of the radiation induced defects in nucleosides and nucleotides, one often sees evidence of damage to the ribose or deoxyribose moiety [37, 48]. Adenosine and deoxyadenosine only differ by substitutions at C2′. This suggests that small changes in the environmental may have a large effect on the trapping site of the oxidative product.

18.5. SIMULATING THE EPR SPECTRA OF DNA

The next step is to use the information obtained from the DNA constituents discussed above to simulate the EPR spectrum of whole DNA. Several groups have contributed to this work. Hüttermann and co-workers have simulated the spectra of oriented DNA using the known EPR/ENDOR hyperfine couplings obtained from model compounds [65, 66]. Sevilla and co-workers have simulated the EPR spectrum of single stranded and double stranded DNA using spectra obtained of $C^{\bullet -}$ from dCMP, $T^{\bullet -}$ from dTMP, $G^{\bullet +}$ from dGMP and $A^{\bullet +}$ from dAMP [67]. The results for whole DNA equilibrated in D_2O, irradiated and observed at 77 K were, on the reduction side 77% $C^{\bullet -}$ and 23% $T^{\bullet -}$, and >90% $G^{\bullet +}$ on the oxidation side.

While the EPR simulations are quite good, there is room for improvements. The simulations haven't included sugar radicals. Sugar radicals had not been detected in DNA when these simulations were performed. The likely reasons for not easily detecting sugar radicals in DNA result from the radicals existing in a wide range of conformations. Adding together various groups of radicals with different hyperfine couplings and anisotropic g-factors gives broad EPR lines that are be difficult to detect [68]. Now however there is good evidence for specific sugar radicals in irradiated DNA.

C1′, and possible C4′ and C5′ sugar radicals have been observed in irradiated hydrated DNA at 77 K [66]. The C1′ sugar radical was reported by Razskazovskii et al. in a DNA double helix [69]. The C1′ was also produced in double stranded DNA at 77 K by photoexcitation of the guanine cation radical [70]. The C3′ radical was reported to be 4.5% of the total radical yield in the duplex (d(CTCTCGAGAG)), x-irradiated and observed at 4 K [71]. It is very likely that the DNA simulations could be improved with the inclusion of a small percentage of these typical sugar radicals.

18.5.1. Radical Yields in DNA

So far we have seen that ionization creates a hole and ejects and electron. In DNA the electron is captured exclusively by the pyrimidine bases while the holes are distributed between guanine and the deoxyribose. The next problem to solve is to determine the free radical yield in DNA and to correlate this yield with the yield of strand breaks. These are very challenging experiments since there are so many factors influencing radicals yield.

First of all one has to separate direct effects from indirect effects. This is most conveniently done by dehydration. Studies show that for less than 13 water molecules per nucleotide residue, direct effects dominate [72]. Then one has to have a system in which one can accurately measure the yield of strand breaks, such as plasmid DNA. Finally one has to have high EPR sensitivity to detect the trapped radicals. This can best be done at Q-band (35 GHz) at helium temperatures. These are the conditions used by Bernhard and co-workers [73].

Bernhard and co-workers have performed a series of experiments to determine the mechanisms of DNA strand breakage by direct ionization of plasmid DNA. A big surprise in this work was the discovery that the total yield of single strand breaks exceeds the yield of trapped sugar radicals. Even at very low hydration levels (2.5 waters per nucleotide residue) nearly 2/3 of the strand breaks are derived from precursors other than deoxyribose radicals [74]. The authors conclude that a majority of the strand breaks observed do not result from dissociative electron capture, homolytic bond cleavage from excited states, or from hydroxyl radical attack. Rather, the authors conclude that doubly oxidized deoxyribose is responsible for the high yield of strand breaks.

18.5.2. Two Electron Oxidations

Free radical processes initiated by ionization of DNA are dominated by combination reactions [75]. When electrons and holes recombine the result is primarily a return to the parent structure, thus resulting in no damage. On the other hand hole-hole combination reactions result in one site being doubly oxidized with the probability of damage at the site being very high.

The first one electron oxidation produces a radical cation on the sugar phosphate ($SP^{\bullet +}$). The radical cation subsequently deprotonates yielding a neutral carbon centered radical $SP(-H)^{\bullet}$. The second oxidation involves an electron transfer from $SP(-H)^{\bullet}$ to a nearby guanine radical cation $G^{\bullet +}$. This step requires that the hole on the guanine have some mobility. It is known that a hole located on guanine at 4 K is mobile, with a range of ca. 10 base pairs [76]. The result of this second oxidation is a a deoxyribose carbocation $SP(-H)^{+}$.

There is lots of current interest in doubly oxidized deoxyribose. A recent article by Roginskaya et al. [77] detected 5-methylene-2-furanone (5-mF) release in irradiated DNA. The production of 5-mF involves C1′ chemistry. To produce 5-mF one needs a doubly oxidized site.

18.6. THEORETICAL CALCULATIONS

18.6.1. Calculating Accurate Hyperfine Coupling Constants

Theoretical calculations have recently played an important role in aiding with free radical assignments. A few years ago the calculation of spin densities and hyperfine

couplings on even small molecules was a very challenging task. Colson et al. reported the spin densities, computed at the HF/6-31G*//HF/3-21G level, for the anions and cations of the four DNA bases [56]. Their results correctly indicated the majors regions of spin density. For example, the major sites of spin density for the adenine reduction product were computed to be $\rho(C2) = 0.71$, $\rho(C8) = 0.03$, and $\rho(N3) = 0.08$. While these are the sites of spin density expected for an adenine reduction product, these results are not very close to the experimentally determined spin densities of $\rho(C2) = 0.41$, $\rho(C8) = 0.14$, and $\rho(N3) = 0.12$ in Section 18.3.5.1.1.

The goal is to make comparisons of calculated and experimental isotropic and anisotropic hyperfine couplings a useful guide in identifying radiation induced free radicals. The basic problem here is that the calculation of accurate hyperfine coupling constants is rather difficult. Two factors are involved: the isotropic component (A_{iso}) (see Eq. 18-2) and the anisotropic component (A_{xx} , A_{yy} , A_{zz}) (See Eq. 18-3). One must have a good description of electron correlation and a well defined basis set in order to calculate accurate isotropic hyperfine couplings. This is not easy to do with molecules the size of the DNA bases. Even when the computational demands are met, the theoretical calculations may deviate more than 20% from the experimental results.

Wetmore et al. have achieved impressive results with the use of Density Functional Theory (DFT) calculations on the primary oxidation and reduction products observed in irradiated single crystals of Thymine [78], Cytosine [79], Guanine [80], and Adenine [81]. The theoretical calculations included in these works estimated the spin densities and isotropic and anisotropic hyperfine couplings of numerous free radicals which were compared with the experimental results discussed above. The calculations involve a single point calculation on the optimized structure using triple-zeta plus polarization functions (B3LYP/6-311G(2df,p)). In many cases the theoretical and experimental results agree rather well. In a few cases there are discrepancies between the theoretical and experimental results.

The discrepancies between experimental and theoretical results have been discussed in a recent review article [82]. This article presents the success and failure of DFT to calculate spin densities and hyperfine couplings of more than twenty primary radiation induced radicals observed in the nucleobases. Several cases are presented here.

To give a specific example one could look at the calculations on the cytosine reduction product. Wetmore et al. calculate that the spin densities for the $C(N3+H)^{\bullet}$ radical are $\rho(C6) = 0.53$, $\rho(N3) = 0.09$, and $\rho(N4) = 0.03$, in good agreement with the experimental results presented in Section 18.3.5.2 [79]. A discrepancy arose however over one of the -N4-H_2 protons which had a calculated hyperfine coupling of 55 MHz which results from the proton on the exocyclic nitrogen being 60.6° out of the molecular plane. No such coupling was observed experimentally. Indeed, as discussed in Section 18.3.5.2, there is good evidence that the radical structure of the $C(N3+H)^{\bullet}$ radical is essentially planar. Calculations with the -N4-H_2 protons

confined to the ring plane were shown to be is much better agreement with the experimental results [82].

Wetmore et al. also examined the oxidation product in cytosine [79]. They computed spin densities $\rho(N1) = 0.29$ and $\rho(C5) = 0.49$ for the N1 deprotonated cation observed in cytosine monohydrate. These results are very close to the experimental results presented in Section 18.4.1.1 $\rho(N1) = 0.30$ and $\rho(C5) = 0.57$. However, since their calculated C5-H isotropic hyperfine coupling (−31.5 MHz) is significantly different from the experimental value (−41.4 MHz), and their calculation predicts only a small N4 spin density, they reject the N1 deprotonated cation model. To see why this is not correct, one can invoke the litany of observations presented above from a radiation chemistry perspective.

First of all the high spin density on C5 is indicative of an oxidation product. In order to be stably trapped, cations have to deprotonate. In cytosine monohydrate, this deprotonation can most easily occur at N1 or N4. Deprotonation at the amino group would give a radical species that would not fit the EPR/ENDOR data. Therefore the N1 deprotonated cation is the best model to represent the experimental data, and actually the best model from the calculations that Wetmore et al. performed [79]. The disagreement Wetmore et al. report is with the C5-H isotropic hyperfine coupling. This is actually to be expected since the authors have not included the important effects of the hydrogen bonded network present in the single crystal in their calculations.

Another example involves calculations on the N3 protonated adenine anion $A(N3+H)^{\bullet}$. Theoretical calculations on the N3 protonated anion yield spin densities of $\rho(N3) = 0.11$, and $\rho(C2) = 0.49$ [81]. Again, in the optimized structure amino group is non-planar with both hydrogen's out of the molecular plane. One of the amino hydrogen's has a hyperfine coupling 43 MHz, something not seen experimentally. Calculations on a planar model yield spin densities of $\rho(N3) = 0.12$, $\rho(C8) = 0.13$ and $\rho(C2) = 0.53$ [82]. These agree nicely with the experimentally determined results presented in Section 18.3.5.1.1. The fully optimized C_s geometry is only 1.7 kcal/mole above the non-planar structure.

As discussed in Section 18.3.5.1.2, the N6 deprotonated adenine cation $A(N3+H)^{\bullet}$, is characterized by $\rho(C8) = 0.16$ and $\rho(N6) = 0.42$. Theoretical calculations on this radical yield spin densities of $\rho(N6) = 0.59$, $\rho(N1) = 0.17$, and $\rho(N3) = 0.23$ [81]. The experimental isotropic hyperfine couplings are N6-H_α = 33.9 MHz, and C8-H_α = 12.4 MHz while the calculated couplings are N6-H_α = 35.8 MHz and C8-H_α = 10.4 MHz, showing satisfactory agreement.

This brings up an important point. The DFT calculations discussed here were performed on isolated molecules, whereas the experimental results reported involve free radical formation in the solid-state, mainly in single crystals. Therefore the theoretical calculations are ignoring the electrostatic environment of the radicals discussed, in particular the intricate hydrogen bonding structure that the free radicals are imbedded in. This often leads to non-planar radicals which may or may not represent what is believed to be observed experimentally.

18.6.2. Improved Basis Sets

The results presented above suggest that DFT calculations at the B3LYP/6-311G(2df,p) give reasonably accurate hyperfine couplings. In the literature there are numerous discussions about refining these calculations. Bartlett and co-workers have discussed the use of coupled cluster methods to compute accurate isotropic hyperfine couplings [83]. Of course some of these couple cluster calculations would be very time consuming for a nucleic acid base.

Barone and co-workers have studied the use of various hybrid density functional for studying the structural and electronic characteristics of organic π-radicals [84]. They conclude that hybrid methods like B3LYP provided good geometries, and good one-electron properties and energetics. A long review article by Improta and Barone has important comments and makes similar conclusions about the use of B3LYP methods to compute hyperfine couplings for the radicals observed in the nucleic acid bases [85]. This article also contains an important discussion on the need for including vibrational averaging effects in these hyperfine coupling calculations. An article by Sieiro and co-workers echo these sentiments about the utility of DFT in a study of ^{14}N isotropic hyperfine couplings. They claim that the B3LYP functional with the 6-31G(d) basis set is actually better than B3LYP with either a TZVP or a cc-pVQZ basis set [86].

Finally, an interesting paper by Tokdemir and Nelson looks at irradiated inosine single crystals [87]. The authors have used calculations on the anisotropic hyperfine couplings as an aid in identifying free radical structures. They find that the computed dipolar coupling eigenvectors correlate well with the experimental results. The input Cartesian coordinates used for the calculations were obtained from the crystallographic data.

18.6.3. Radical Stability

Another problem that can be addressed by theoretical calculations has to do with radical stability. Since radiation scatters electrons from different molecular orbitals at random, one might expect to see a great variety of damaged products. Usually this is not the case, as discussed in Section 18.2. Theoretical calculations are useful here in ranking the energies of the various oxidation and reduction products. It is often possible therefore to predict which products will be observed in a particular system.

These ideas have been illustrated in a recent study of the co-crystalline complex of 1-MethylCytosine:5-FluoroUracil [34]. Using model calculations it was shown how the hydrogen bonding network of the crystal is able to sustain a proton shuttle which leads to the selective formation of certain radicals. Calculations were able to predict that the site of reduction would be the cytosine base (yielding the N3 protonated cytosine anion $C(N3+H)^{\bullet}$.), while the uracil base would be the site of oxidation (yielding the N1 deprotonated uracil cation $U(N1-H)^{\bullet}$). These are indeed the primary radiation induced species observed experimentally [34, 88]. The results also nicely agree with the model proposed for radical trapping by Bernhard [11].

18.6.4. Calculations on Larger Systems

In order to understand the effects of radiation damage to DNA it is necessary to consider larger model systems such as nucleotides, base pairs, and stacked bases. The question then becomes whether or not it is possible to do reliable calculations on such large systems. The literature is full of various attempts to study these complex systems. Some attempts have been more successful than others.

For example, there are many studies that claim a discrepancy between theoretical and experimental Watson-Crick hydrogen bond lengths. Calculations by Bertran et al. [89] and Santamaria et al. [90] seem to be in good agreement with the experimental data for the AT base pair, but their geometries differ significantly from the experimental geometries for the GC base pair. This work was followed with a report by Bickelhaupt et al. that claimed this discrepancy resulted from neglect of waters of hydration, sugar hydroxyl groups, and Na^+ counterions [91]. More recent MP2 optimizations have produced nonplanar geometries for the GC base pair, and planar geometries for the AT base pair [92].

18.6.5. Calculations of Ionization Potentials

In the experimental sections there was much discussion about products formed after one-electron loss. For example, ionization of DNA is a random process, yet 90% of the radical cations end up on guanine (which has the lowest gas-phase ionization potential). This brings up several questions that can be answered by theoretical calculations.

First of all, can one verify that guanine has the lowest gas-phase ionization potential? Does guanine have the lowest ionization potential in aqueous solution? Are there arrangements of several stacked bases that may be more easily oxidized than guanine? Are there situations when the deoxyribose or the phosphate may be oxidized, say in a nucleotide?

Some time ago, Sevilla and co-workers calculated the adiabatic ionization potentials of the DNA bases at the MP2/6-31+G(d) level. They showed that the ionization potentials are within 0.1 eV of the experimental values and that the order is as expected T>C>A>G [93]. More recently, others have repeated these calculations. Wetmore et al. reported similar results with B3LYP/6-311+G(2df,p) [94]. Recent calculations have shown problems with spin contamination in the radical cations using MP2 calculations which are greatly improved by using projected MP2 energies (PMP2) [95]. This work also looks at the influence of the deoxyribose on the ionization potentials. A new paper by Roca-Sanjuán et al. calculates the vertical and adiabatic ionization potentials for the bases using MP2, multiconfigurational perturbation theory (CCSD(T)), and coupled cluster theory [96]. This paper has useful tables which summarize the range of the experimental values, and presents calculations that are within the experimental range.

Calculations of the ionization potentials of the DNA bases have been reported using a polarized continuum model [95]. The results are seen to nicely agree with

the experimental results reported by LeBreton et al. [97]. It is interesting to note that the order T>C>A>G of the ionization potentials is preserved in these calculations.

There is considerable interest in knowing if the ease of oxidation of guanine residues by ionizing radiation is sensitive to variations of base sequence. Saito et al. have shown experimentally that the trend in ionization potentials is 5′-GGG-3′ < 5′-GG-3′ < 5′-GA-3′, < 5′-GT-3′ ~ 5′-GC-3′ <G [98]. Theoretical calculations by Sugiyama and Saito showed that the HOMO of a GG stack is especially high in energy and concentrated on the 5′-G [99]. Prat et al. have done theoretical calculations on GG stack with the inclusion of 8-oxyguanine. They find that the ionization potential drops nearly 0.5 eV when 8-oxyguanine is stacked with guanine [100]. Another experimental and theoretical article by Saito and co-workers considers larger stack, such as 5′-TGGT-3′ and 5′-CGGGC-3′ [101]. This work used only a HF/6-31G(d) level of theory, did not optimize the structures, and reports only the Koopmans' ionization potentials.

Schuster's group has reported interesting new experimental and theoretical results on oligonucleotides. A paper by Barnett et al. reports on a duplex of d(5′-GAGG-3′)•d(3′-CTCC-5′) [102]. The authors have included forty eight solvating water molecules and six Na^+ counterions in their calculations. The results show that the ionization potential and the position where the radical cation is localized are strongly modulated by the location of the counterions. In a second report, the authors show that the level of hydration also influences the ionization potential and the position where the radical cation is localized [103]. Both these studies have very interesting color pictures of the orbital isosurfaces which show hole distribution mainly on the GG pair, but with some delocalization onto the sugar-phosphate and the water molecules. This delocalization may explain why the authors see an increase in the vertical ionization potential of the hydrated model.

There are now several groups with sufficient computer power to do high level calculations on nucleotides. Schaefer and co-workers have performed calculations on the 2′-deoxyadenosine-5-phosphate anion [104]. This is labeled an anion since a net negative charge resides on the phosphate. Therefore one electron oxidation produces a neutral molecule. The vertical detachment energy is computed to be 5.23 eV (the experimental value is 6.05 eV [105]). These values may not be of interest to studies of DNA since in DNA the negative charge on the phosphate is neutralized by a counterion. This paper also shows the spin density for the radical resides on both the base adenine and the phosphate. Again this most likely will not occur in DNA. In DNA one electron oxidation produces a radical cation that would reside wholly on the adenine, and would rapidly deprotonate to give the A(N6-H)• radical as outlined in Section 18.4.1.4. There have been recent papers on the influence of discrete waters on the ionization potentials of the DNA bases. Experimental work by Kim et al. [106] showed that the ionization potential of thymine is reduced by 0.3 eV using a single bound water, while a second water decreases the ionization potential a further 0.2 eV. Recent calculations on the canonical form of thymine showed much smaller decreases in the vertical ionization potential with the addition of discrete waters of hydration [107, 108].

18.6.6. Calculations of Electronic Affinities

There are several recent studies involving electron adducts to nucleotides. The primary emphasis recently has been on modeling strand breaks through dissociative electron attachment (see Section 18.1.3).

In a report by Gu et al. 2′-deoxycytidine-3′-monophosphate is charge neutralized by a single proton on the phosphate [109]. The vertical electron attachment energy is calculated to be 0.15 eV, suggesting that 3′-dCMPH can capture near 0 eV electrons. The SOMO of the radical anion is seen to reside solely on the cytosine base.

The first attempts to model dissociative electron attachment were by Simons and co-workers in 5′-dCMP [110]. These calculations were later refined by Leszczynski and coworkers who report that it requires ca. 14 kcal/mole to dissociate the C5′-O5′ bond in both 5′-dCMP and in 5′-dTMP [111]. Both of these studies begin with the trapped electron in a π-orbital on the base. This presents a problem from the perspective of radiation chemistry given that in an aqueous environment, when an electron is stabilized in the π-orbital of a base, no significant amount of stand breakage is observed [2].

It seems as if this problem can be solved by considering mechanisms that occur before the electron has time to fully relax. The idea being that transient anions associated with the lowest unoccupied molecular orbitals will excite vibrational modes. These ideas are outlined in a new paper by Kumar and Sevilla that looks at C5′-O5′ bond dissociation in 5′-dTMP. They report that on the vertical potential energy surface, the B3LYP/6-31G(d) calculated barrier height for C5′-O5′ bond dissociation is ca. 9 kcal/mole which is lower than the adiabatic value for this same process [112].

18.7. CONCLUSIONS

This review has spanned many years of work devoted to the attempts to understand the effects of radiation damage to DNA. The emphasis has been on the use of EPR/ENDOR spectroscopy to reveal the structures of the primary radiation induced products in DNA. ENDOR was invented before 1960, but it took quite some time before this technique was used to study problems in radiation biology. The basic reason is that complex equipment had to be designed and tested that permits the irradiation and examination of small single crystals at helium temperatures. The apparatus was only completed around 1975 by Bernhard and co-workers in Rochester, and by Hüttermann and co-workers in Regensburg.

Once work described here was completed on the nucleotides and nucleosides, it was not easy to extend this work to oligonucleotides. This step required years of work to produce even very small single crystals. The crystals turned out to be too small to use in the X-band Cryo-Tip apparatus described in Section 18.3.1. Thus, a great deal more time had to be devoted to building helium temperature apparatus at higher microwave frequencies (Q-band). This task has only recently been completed. Now we have the exciting new results discussed in Section 18.5.2. However, there is much that remains to be done.

18.7.1. Directions for Future Work

In the discussions above about the complex systems studied, there were comments suggesting that further studies would be helpful. These suggestions for future work are collected below.

In the section on model compounds there are discussions about thymine, cytosine and guanine nucleotides. To date there have been no detailed EPR/ENDOR experiments on an adenine nucleotide because of the inability to grow good single crystals. The structure of 5′-dAMP hexahydrate is known from a crystal structure study [113]. It would be very interesting to analyze the primary radiation induced products in 5′-dAMP at helium temperature to see if there is actually spin density on both the phosphate and the adenine base for the oxidation product as reported in the theoretical study by Hou et al. [104].

The discussion in Section 18.4.1.4 on adenine mentions that the radiation chemistry of the two nucleosides adenosine and deoxyadenosine are very different. In adenosine one observes the A(N6-H)$^{\bullet}$ radical, while in deoxyadenosine the site of oxidation is on the deoxyribose. These two structures differ only at the C2′ position. A small environmental change in the crystal structure seems to have a large effect on the trapping site of the oxidative product. It would be very interesting to know just what small changes in the environment are important here.

Early EPR work on sugar radicals led to some questionable radical assignments. There is a need to repeat some of these studies with EPR/ENDOR spectroscopy. It is therefore very encouraging to see new papers in this field with titles like "Q-band EPR and ENDOR of Low Temperature X-Irradiated β-D-Fructose Single Crystals" [114] which is using all of the techniques described here to great advantage.

The discussion in Section 18.5 on simulations of the EPR spectra of DNA mentioned room for improvements. It would be very interesting to add new structures discussed herein to the simulations. New simulations should include sugar radicals, accurate hyperfine couplings from the EPR/ENDOR studies, perhaps an adenine oxidation product, and the oxidation product in 5-MeCytosine. Some of the DNA simulations Hüttermann and co-workers performed included the thymine allyl radical [23]. This assignment seemed improbable at the time since oxidation of thymine is not expected in DNA. It would be interesting to know if this allyl component used in the simulations might actually be from an oxidized 5-MeCytosine.

Methylation of cytosine residues within CpG dinucleotides is important in the regulation of genes. The interest in 5-MeCytosine results from its low ionization potential. It would be very interesting to continue the work on GG stacks (Section 18.6.4) by including 5-MeCytosine in the ionization potential calculations.

In the section on theoretical calculations it was mentioned that calculations on the influence of discrete waters of hydration on the ionization potential of thymine are at odds with experimental results (Section 18.6.5). It is important to carry out further calculations on discrete waters of hydration in light of a new article by van Mourik and co-workers [115] which suggests that the hydration shell of thymine may be much more complicated than generally assumed.

The recent work on two one-electron oxidations of a single deoxyribose (Section 18.5.2) is very interesting. It is important for experimentalists to design new tests for the occurrence of two one-electron oxidations at a single site. It is also important to model the energetics of this process in a number of different environments.

Finally, it should be obvious that ENDOR spectroscopy should be very useful in studying radiation damage to oligonucleotides or even whole DNA. While several investigators have tried these experiments, there are to date no published results showing ENDOR signals in DNA.

ACKNOWLEDGMENTS

As it is true that none of us is as smart as we are together, it is important to note that much of this review covers work I've done in collaboration with the following people. From 1974–1978, I was a National Institutes of Health, Post-Doctoral Research Fellow at the University of Rochester, Department of Radiation Biology. I worked with Bill Bernhard doing low temperature EPR/ENDOR studies on nucleotides. In the early 1980s I began collaborations with Bill Nelson at Georgia State University, Department of Physics and with Einar Sagstuen at the University of Oslo, Biophysics Department. Much of this work was supported by PHS Grant R01 CA36810 awarded by the National Cancer Institute, DHHS. Recently I've begun theoretical calculations on the nucleic acid bases. Help in learning this new field from Leonid Gorb, Jackson State University, and Carlos Crespo-Hernández, Case Western Reserve, is greatly appreciated.

REFERENCES

1. von Sonntag C, Schuchmann H-P (1986) Int J. Radiat Biol 49: 1.
2. von Sonntag C (1987) The Chemical Basis of Radiation Biology. Taylor and Francis, London, New York, Philadelphia.
3. Bernhard WA (1981) Advan Radiat Biol 9: 199.
4. Close DM (1993) Radiat Res 135: 1.
5. Steenken S (1992) Free Radical Res Comm 16: 349.
6. Steenken S, Telo JP, Novais HM, Candeias LP (1992) J Am Chem Soc 114: 4701.
7. von Sonntag C (2006) Free-Radical-Induced DNA Damage and Its Repair: A Chemical Perspective. Springer-Verlag, New York.
8. Boudaiffa B, Cloutier P, Hunting D, Huels MA, Sanche L (2000) Science 287: 1658.
9. Krisch RE, Flick MB, Trumbore CN (1991) Radiat Res 126: 251.
10. O'Neill P (2001) In: Jonah, CD, Rao BSM (eds) Radiation Chemistry; Present Status and Future Trends. Elsevier, Amsterdam.
11. Bernhard WA, Barnes J, Mercer KM, Mroczka N (1994) Radiat Res 140: 199.
12. Close DM, Mengeot M, Gilliam OR (1981) J Chem Phys 74: 5497.
13. Weil JA, Schindler P, Wright PM (1967) Rev Sci Instr 38: 659.
14. Air-Products LT-3-110 Heli-Tran System, Air Products. Allentown, PA.
15. Mercer KR, Bernhard WA (1987) J Magn Reson 74: 66.

16. Atherton NM (1973) Electron Spin Resonance; Theory and Applications. John Wiley and Sons, New York.
17. Wertz JE, Bolton JR (1972) Electron Spin Resonance; Elementary Theory and Practical Applications. McGraw-Hill, New York.
18. McConnell HM, Chesnut DB (1958) J Chem Phys 28: 107.
19. McConnell HM, Heller C, Cole T, Fessenden RW (1960) J Amer Chem Soc 82: 766.
20. Miyagawa I, Gordy W (1960) J Chem Phys 32: 255.
21. Lund A, Vänngård T (1965) J Chem Phys 59: 2484.
22. Busing WR, Martin KO, Levy HA (1964) Oak Ridge National Laboratories. ONRL-TM-306.
23. Weiland B, Hüttermann J, van Tol J (1997) Acta Chemica Scand 51: 585.
24. Feher G (1956) Phys Rev 103: 834.
25. Feher G (1959) Phys Rev 114: 1219.
26. Kevan L, Kispert LD (1976) Electron Spin Double Resonance Spectroscopy. John Wiley and Sons, New York.
27. Schonland DS (1959) Proc Phys Soc London, Sect A 73: 788.
28. Andersen MF, Sagstuen E, Henriksen T (1987) J Magn Reson 71: 461.
29. Sagstuen E, Close DM, Vagane R, Hole EO, Nelson WH (2006) J Phys Chem A 110: 8653.
30. Close DM, Nelson WH (1989) Radiat Res 117: 367.
31. Chacko VP, McDowell CA, Singh BC (1979) Mol Phys 38: 321.
32. Nelson WH, Gill C (1978) Mol Phys 36: 1779.
33. Bernhard WA (1984) J Chem Phys 81: 5928.
34. Close DM, Eriksson LA, Hole EO, Sagstuen E, Nelson WH (2000) J Phys Chem B 104: 9343.
35. Broomhead JM (1950) Acta Crystall 4: 92.
36. Close DM, Sagstuen E, Nelson WH (1985) J Chem Phys 82: 4386.
37. Hole EO, Nelson WH, Sagstuen E, Close DM (1992) Radiat Res 129: 119.
38. Hole EO, Sagstuen E, Nelson WH, Close DM (1992) Radiat Res 129: 1.
39. Lefebvre R, Maruani J (1965) J Chem Phys 42: 1480.
40. Lefebvre R, Maruani J (1965) J Chem Phys 42: 1496.
41. Sagstuen E, Lund A, Itagaki Y, Maruani J (2000) J Phys Chem A 104: 6362.
42. Sornes AR, Sagstuen E, Lund A (1995) J Phys Chem 99: 16867.
43. Close DM, Hole EO, Sagstuen E, Nelson WH (1998) J Phys Chem 102: 6737.
44. Barnes JP, Bernhard WA (1994) J Phys Chem 98: 887.
45. Sagstuen E, Hole EO, Nelson WH, Close DM (1992) J Phys Chem 96: 8269.
46. Close DM, Fouse GW, Bernhard WA (1977) J Chem Phys 66: 4689.
47. Close DM (2003) J Phys Chem B 107: 864.
48. Hole EO, Sagstuen E, Nelson WH, Close DM (1991) J Phys Chem 95: 1494.
49. Sagstuen E, Hole EO, Nelson WH, Close DM (1992) J Phys Chem 96: 1121.
50. Sevilla MD (1971) J Phys Chem 75: 626.
51. Candeias LP, Wolf P, O'Neill P, Steenken S (1992) J Phys Chem 96: 10302.
52. Hole EO, Sagstuen E, Nelson WH, Close DM (1991) Radiat Res 125: 119.
53. Bachler V, Hildenbrand K (1992) Radiat Phys Chem 40: 59.
54. Reynisson J, Steenken S (2002) Phys Chem Chem Phys 4: 527.
55. Candeias LP, Steenken S (1989) J Amer Chem Soc 111: 1094.
56. Colson AO, Besler B, Close DM, Sevilla MD (1992) J Phys Chem 96: 661.
57. Mundy CJ, Colvin ME, Quong AA (2002) J Phys Chem A 106: 10063.
58. Hutter M, Clark T (1996) J Am Chem Soc 118: 7574.
59. Li X, Cai Z, Sevilla MD (2001) J Phys Chem B 105: 10115.
60. Jayatilaka N, Nelson WH (2007) J Phys Chem B 111: 800.

61. Adhikary A, Kumar A, Becker D, Sevilla MD (2006) J Phys Chem B 110: 24171.
62. Nelson WH, Sagstuen E, Hole EO, Close DM (1992) Radiat Res 131: 10.
63. Nelson WH, Sagstuen E, Hole EO, Close DM (1998) Radiat Res 149: 75.
64. Close DM, Nelson WH, Sagstuen E, Hole EO (1994) Radiat Res 137: 300.
65. Hüttermann J, Voit K, Oloff H, Kohnlein W, Gräslund A, Rupprecht A (1984) Disc Farad Soc 78: 135.
66. Weiland B, Hüttermann J (1998) Int J Radiat Biol 74: 341.
67. Sevilla MD, Becker D, Yan M, Summerfield SR (1991) J Phys Chem 95: 3409.
68. Close DM (1997) Radiat Res 147: 663.
69. Razskazovskii Y, Roginskaya M, Sevilla MD (1998) Radiat Res 149: 422.
70. Shukla LI, Pazdro R, Huang J, DeVreugd C, Becker D, Sevilla MD (2004) Radiat Res 161: 582.
71. Debije MG, Bernhard WA (2001) Radiat Res 155: 687.
72. Debije MG, Strickler MD, Bernhard WA (2000) Radiat Res 154: 163.
73. Purkayastha S, Milligan JR, Bernhard WA (2005) J Phys Chem B 109: 16967.
74. Purkayastha S, Milligan JR, Bernhard WA (2006) J Phys Chem B 110: 26286.
75. Bernhard WA, Mroczka N, Barnes J (1994) Int J Radiat Biol 66: 491.
76. Debije MG, Bernhard WA (2000) J Phys Chem B 104: 7845.
77. Roginskaya M, Razskazovskiy Y, Bernhard WA (2005) Angew Chem Int Ed 44: 6210.
78. Wetmore SD, Boyd RJ, Eriksson LA (1998) J Phys Chem B 102: 5369.
79. Wetmore SD, Himo F, Boyd RJ, Eriksson LA (1998) J Phys Chem B 102: 7484.
80. Wetmore SD, Boyd RJ, Eriksson LA (1998) J Phys Chem B 102: 9332.
81. Wetmore SD, Boyd RJ, Eriksson LA (1998) J Phys Chem B 102: 10602.
82. Close DM (2003) In: Leszczynski J (ed) Computational Chemistry: Reviews of Current Trends, Vol 8. World Scientific, Singapore.
83. Fau S, Bartlett RJ (2003) J Phys Chem A 107: 6648.
84. Adamo C, Barone V, Fortunelli A (1995) J Chem Phys 102: 384.
85. Improta R, Barone V (2004) Chem Rev 104: 1231.
86. Hermosilla L, Calle P, García de la Vega JM, Sieiro C (2006) J Phys Chem A 110: 13600.
87. Tokdemir S, Nelson WH (2006) J Phys Chem A 110: 6552.
88. Close DM, Farley RA, Bernhard WA (1978) Radiat Res 73: 212.
89. Bertran J, Oliva A, Rodriguez-Santiago L, Sodupe M (1998) J Am Chem Soc 120: 8159.
90. Santamaria R, Vaquez A (1994) J Comput Chem 15: 981.
91. Guerra CF, Bickelhaupt FM, Snijders JG, Baerends EJ (2000) J Am Chem Soc 122: 4117.
92. Kurita N, Danilov VI, Anisimov VM (2005) Chem Phys Letts 404: 164.
93. Sevilla MD, Besler B, Colson AO (1995) J Phys Chem 99: 1060.
94. Wetmore SD, Boyd RJ, Eriksson LA (2000) Chem Phys Lett 322: 129.
95. Close DM (2004) J Phys Chem A 108: 10376.
96. Roca-Sanjuán D, Rubio M, Merchán M, Serrano-Andrés L (2006) J Chem Phys 125: 084302.
97. Fernando H, Papadantonakis GA, Kim NS, LeBreton PR (1998) Proc Natl Acad Sci USA 95: 5550.
98. Saito I, Takayama M, Sugiyama H, Nakatani K (1995) J Am Chem Soc 117: 6406.
99. Sugiyama H, Saito I (1996) J Am Chem Soc 118: 7063.
100. Prat F, Houk KN, Foote CS (1998) J Am Chem Soc 120: 845.
101. Yoshioka Y, Kitagawa Y, Takano Y, Yamaguchi K, Nakamura T, Saito I (1999) J Am Chem Soc 121: 8712.
102. Barnett RN, Cleveland CL, Joy A, Landman U, Schuster GB (2001) Science 294: 567.
103. Barnett RN, Cleveland CI, Landman U, Boone E, Kanvah S, Schuster GB (2003) J Phys Chem A 107: 3525.

104. Hou R, Gu J, Xie Y, Yi X, Schaefer HF (2005) J Phys Chem B 109: 22053.
105. Yang X, Wang X, Vorpagel ER, Wang L (2004) Proc Natl Acad Sci USA 95: 5550.
106. Kim SK, Lee W, Herschbach DR (1996) J Phys Chem 100: 7933.
107. Close DM, Crespo-Hernández CE, Gorb L, Leszczynski J (2005) J Phys Chem A 109: 9279.
108. Close DM, Crespo-Hernández CE, Gorb L, Leszczynski J (2006) J Phys Chem A 110: 7485.
109. Gu J, Xie Y, Schaefer HF (2006) J Am Chem Soc 128: 1250.
110. Barrios R, Skurski P, Simons J (2001) J Phys Chem A 108: 7991.
111. Bao X, Wang J, Gu J, Leszczynski J (2006) Proc Natl Acad Sci USA 103: 5658.
112. Kumar A, Sevilla MD (2007) J Phys Chem B 111: 5464.
113. Reddy BS, Viswamitra MA (1975) Acta Cryst B31: 19.
114. Vanhaeleyn GCAM, Pauwels E, Callens FJ, Waroquier M, Sagstuen E, Matthys PFAE (2006) J Phys Chem A 110: 2147.
115. Danilov VI, van Mourik T, Poltev VI (2006) Chem Phys Lett 429: 255 .